AIAA JOURNAL
Vol. 43, No. 9, September 2005

Large-Eddy Simulation of Subsonic Turbulent Jets and Their Radiated Sound

Niklas Andersson,* Lars-Erik Eriksson,† and Lars Davidson†
Chalmers University of Technology, SE-412 96 Göteborg, Sweden

Large-eddy simulations of a compressible nozzle/jet configuration have been carried out. Two jets were simulated, an isothermal jet and a jet with a higher temperature than the quiescent surrounding air. The Mach number was in both cases 0.75, and the jet Reynolds number was 5.0×10^4. Sound pressure levels in far-field observer locations were evaluated using Kirchhoff surface integration. The Favre filtered Navier–Stokes equations were solved using a finite volume method solver with a low-dissipation third-order upwind scheme for the convective fluxes, a second-order centered difference approach for the viscous fluxes, and a three-stage second-order Runge–Kutta technique in time. The computational domain was discretized using a block structured boundary-fitted mesh with approximately 3.0×10^6 cells. The calculations were performed on a parallel computer, using message-passing interface. A compressible form of Smagorinsky's subgrid-scale model was used for computation of the subgrid-scale stresses. Absorbing boundary conditions based on characteristic variables were adopted for all free boundaries. Velocity components specified at the entrainment boundaries were estimated from corresponding Reynolds-averaged Navier–Stokes calculations, which enable the use of a rather narrow domain. This, furthermore, ensures that the correct amount of fluid is entrained into the domain. Two-point space–time correlations were obtained for locations in the shear layer center, from which length and timescales of turbulence structures were evaluated. Predicted near-field flow statistics and far-field sound pressure levels (SPL) are both in good agreement with experiments. Predicted SPL are for all observers locations, where evaluated, within a 3.0-dB deviation from measured levels and for most locations within a 1.0-dB deviation. Experimental data used for validation were provided by Laboratoire d'Etude Aerodynamiques, Poitiers, France.

Nomenclature

C_p	=	specific heat at constant pressure
C_R, C_I	=	Smagorinsky model coefficients
c	=	speed of sound
D_j	=	nozzle outlet diameter
e	=	energy
f	=	frequency
k	=	kinetic energy
$\mathcal{L}$	=	integral length scale
L_c	=	potential core length
M	=	Mach number
Pr	=	Prandtl number
p	=	pressure
$\boldsymbol{Q}$	=	state vector
q_j	=	energy diffusion vector
$\mathcal{R}$	=	correlation amplitude
r	=	radial coordinate or distance from source to observer
Re_D	=	Reynolds number based on the jet diameter
S_{ij}	=	strain rate tensor
Sr	=	Strouhal number, $(fD_j)/U_j$
T	=	temperature
$\mathcal{T}$	=	integral timescale
t	=	time
(u, v, w)	=	axial, radial, and tangential velocity component
$\boldsymbol{u}_i$	=	Cartesian components of velocity vector
$\boldsymbol{x}$	=	flowfield location
x_i	=	Cartesian coordinate vector component
$\boldsymbol{y}$	=	observer location
Δ	=	filter width
δ_{ij}	=	Kronecker delta
θ	=	angle from the x axis
μ	=	dynamic viscosity
ξ	=	spatial separation
ρ	=	density
σ_{ij}	=	viscous stress tensor
τ	=	temporal separation
τ_{ij}	=	subgrid-scale stress tensor
τ_r	=	retarded time
$\langle\ldots\rangle_\theta$	=	circumferentially averaged quantity
$\langle\ldots\rangle_t$	=	time-averaged quantity

Subscripts

j	=	jet, nozzle-exit condition
t	=	turbulent quantity
0	=	total condition
∞	=	freestream or ambient conditions

Superscripts

SGS	=	subgrid scale
$-$	=	spatially filtered quantity
$'$	=	resolved fluctuation
$\sim$	=	spatially Favre-filtered quantity
$\wedge$	=	Fourier transform

Presented as Paper 2004-3024 at the AIAA/CEAS 10th Aeroacoustics Conference, Manchester, England, United Kingdom, 10–12 May 2004; received 7 September 2004; revision received 8 February 2005; accepted for publication 10 February 2005.

*Ph.D. Student, Department of Applied Mechanics, Division of Fluid Dynamics. Student Member AIAA.

†Professor, Department of Applied Mechanics, Division of Fluid Dynamics.

I. Introduction

THE number of commercial aircraft in service is continuously increasing, and airports around the world are growing in size. Moreover, new airports are often built in the vicinity of cities. Restrictions of noise levels in the surroundings of airports have made the reduction of near-ground operation noise an important issue for aircraft and engine manufacturers, and noise generation has now become an important design parameter that is taken into consideration early in the construction process. Flow-induced aircraft noise can

be divided into two categories: airframe noise and noise generated by the jet engine. The first category includes noise generated by landing gear, high-lift devices, and the aircraft fuselage itself, and the second includes turbomachinery noise, core noise, and jet noise. At takeoff, the main sources of noise are the propelling jet and the engine fan, of which the jet exhaust is usually the strongest noise source at full power. In commercial aircraft, increasing the bypass ratio, that is, the ratio of air passing through the engine in the bypass duct to the air passing through the engine core, has given a significant reduction in aircraft noise. However, although increasing the bypass ratio leads to reduced noise levels, the major motivation for this development has not been noise reduction. Rather, the development towards more efficient engines has led to the use of a higher bypass ratio with noise reduction as a positive side effect. The lower noise levels of high-bypass ratio engines are directly attributable to the reduction in jet noise resulting from lower jet velocities. Unfortunately, without a step change in technology the maximum bypass ratio is limited by a number of factors, for example, the length of the fan blades, rotor speed, and engine nacelle drag, and large engines are currently very close to this limit. Consequently, the possibility for reducing jet noise by increasing the bypass ratio is rapidly decreasing.

New noise-reducing concepts will arise from a better understanding of the source mechanisms. For evaluation of the performance of these new concepts, reliable methods for modeling of the source mechanisms must be available. The work presented in this paper has been done within a European Union (EU) project, JEAN (Jet Exhaust Aerodynamics and Noise, EU 5th Framework Project, Contract G4RD-CT2000-000313), that focused on investigating jet noise both numerically and experimentally. Various known methodologies for noise prediction were tested in the project and compared for a few test cases.

Using a grid fine enough in the far-field regions to minimize the introduction of sound propagation errors, the acoustic field can be obtained directly from the flowfield simulation. This requires a detailed numerical compressible flow simulation, for example, direct numerical simulation (DNS), for example, see Freund[1] and Mitchell et al.[2] or large-eddy simulation (LES), as done by, for example, Bogey et al.[3] and Mankbadi et al.[4] With the computational resources available today, DNS is restricted to flows with fairly low Reynolds number. Moreover, it is believed[5] that large scales are more efficient than small ones in generating sound, which justifies the use of LES for sound predictions. Although it is possible to obtain the acoustic signature directly from the flow simulation, resolving the entire acoustic field is computationally expensive. To lower the computational costs, a hybrid approach can be used in which the computational problem is divided into two parts. An LES can be used to obtain the unsteady nonlinear near field, which in the jet-noise case corresponds to the hydrodynamic jet region. The acoustic field is then extended to far-field observer locations using, for example, Kirchhoff surface integration (see Freund et al.[6]).

The feasibility of using LES for both the flowfield and the radiated sound from a high subsonic 6.5×10^4 Reynolds number jet has been discussed by Bogey et al.[3,7,8] In Refs. 3 and 7, the acoustic field was obtained directly from the flow simulation. Noise-generation mechanisms were found to be relatively independent of Reynolds number. In Ref. 8, Lighthill's[9] acoustic analogy was used in combination with compressible LES to obtain the acoustic field. Bogey and Bailly[10] investigated the effects of inflow conditions on the flowfield and the radiated sound of a high-Reynolds-number, $Re_D = 4.0 \times 10^5$, Mach 0.9 jet. Both the flow development and the emitted sound were shown to depend appreciably on initial parameters. Bodony and Lele[11] investigated the changes in jet mean field and far-field sound with temperature and Mach number. Results where found to be in agreement with published data.[12] Freund[1] investigated sources of sound in a Mach 0.9 jet at a Reynolds number of $Re_D = 3.6 \times 10^3$ using DNS. In this work the part of the Lighthill source that can radiate to the far field was isolated using Fourier methods. It was found that the peak of the radiating source coincides with neither the peak of the total source nor the peak of turbulence kinetic energy. Shur et al.[13] made simulations of a cold Mach 0.9 jet at a Reynolds number of 1.0×10^4. Radiated sound was successfully predicted using the Ffowcs Williams–Hawkings[14] surface integral formulation. The simulation was conducted using only 5.0×10^5 cells. This work was done using the monotone-integrated LES approach, where the subgrid-scale model, essentially, is replaced by the numerical dissipation of the numerical method used. Zhao et al.[15] conducted an LES of a Mach 0.9 jet at Reynolds number 3.6×10^3 and a jet at Mach 0.4 and a Reynolds number of 5.0×10^3. In this study, radiated sound was obtained both directly from the LES and by using Kirchhoff surface integration. The effect on the radiated sound of the subgrid-scale model used was investigated. It was found that using a mixed subgrid-scale model resulted in both higher turbulence levels and sound levels.

II. Overview of the Present Study

Large-eddy simulations of a Mach 0.75 nozzle/jet configuration were performed. The Reynolds number based on the nozzle-exit diameter and the jet velocity at the nozzle-exit plane Re_D was 5.0×10^4. The Reynolds number in the measurements by Jordan et al.[16,17] and Jordan and Gervais,[18] used for comparison and validation of the simulations, was approximately 7.5×10^5. Such a high Reynolds number probably means that the scales that need to be resolved are too small. Thus the Reynolds number in our LES was decreased with the assumption that the flow is only weakly Reynolds number dependent. This Reynolds-number reduction will affect the turbulence in the initial region and thus the frequency content of the radiated sound. However, the differences will probably be most noticeable in the high-frequency regime and thus not very important here because these high frequencies are to a high degree filtered by the numerics and therefore not included in the analysis.

Simulations of the Mach 0.75 jet were performed for two flow conditions: an unheated jet, that is, a jet where the static temperature in the nozzle-exit plane T_j was equal to the static temperature of the ambient air T_∞ and a heated version in which the exhaust temperature was twice that of the surrounding air. The main reason for choosing the Mach 0.75 jet was that experimental data were available for both isothermal and heated conditions. This made it possible to investigate whether heating effects on both the flowfield and on the radiated sound could be accurately captured with the LES/Kirchhoff approach. Furthermore, both the jet Mach number and the temperature ratio used for the heated jet are quite realistic for real jet engines. Table 1 gives flow properties defining the flowfields of the two jets simulated. Differences are highlighted using boldface numbers. The two jets, that is, the isothermal and heated Mach 0.75 jet, will hereafter be referred to as jet 1 and jet 2, respectively.

The nozzle geometry used for the simulations corresponds to the last contraction of the nozzle configuration in the experimental setup.

The measurements were made by Jordan et al.[16,17] and Jordan and Gervais[18] at the MARTEL facility of Centre d'Etudes Aerodynamiques et Thermiques, Poitiers, France. The measurements have also been reported by Power et al.[19] Two-component single-point and monocomponent two-point measurements were made using laser Doppler velocimetry. The acoustic field was sampled using an arc of microphones at 30 jet diameters and 50 jet diameters from the jet exit, respectively. For more detail on the experimental setup, see Jordan et al.[16,17] and Jordan and Gervais.[18]

Table 1 Flow properties

Parameter	Jet 1	Jet 2
U_j/c_∞	0.75	0.75
T_j/T_∞	**1.0**	**2.0**
P_∞, Pa	101,300	101,300
ρ_∞, kgm^{-3}	1.225561	1.225561
c_∞, ms^{-1}	340.174	340.174
U_∞, ms^{-1}	0.0	0.0
T_∞, K	288.0	288.0
T_{0_j}, K	**320.4**	**608.4**
Re_D[a]	5.0×10^4	5.0×10^4

[a]The Reynolds number was decreased using modified viscosity.

III. Governing Equations

The equations solved are the spatially Favre-filtered continuity, momentum, and energy equations,

$$\frac{\partial \bar{\rho}}{\partial t} + \frac{\partial(\bar{\rho}\tilde{u}_i)}{\partial x_i} = 0 \tag{1}$$

$$\frac{\partial(\bar{\rho}\tilde{u}_i)}{\partial t} + \frac{\partial(\bar{\rho}\tilde{u}_i\tilde{u}_j)}{\partial x_j} = -\frac{\partial \bar{p}}{\partial x_i} + \frac{\partial \bar{\sigma}_{ij}}{\partial x_j} + \frac{\partial \tau_{ij}}{\partial x_j} \tag{2}$$

$$\frac{\partial(\bar{\rho}\tilde{e}_0)}{\partial t} + \frac{\partial(\bar{\rho}\tilde{e}_0\tilde{u}_j)}{\partial x_j} = -\frac{\partial \bar{p}\tilde{u}_j}{\partial x_j} + \frac{\partial}{\partial x_j}\left(C_p\frac{\mu}{Pr}\frac{\partial \tilde{T}}{\partial x_j} + q_j\right) + \frac{\partial}{\partial x_j}[\tilde{u}_i(\bar{\sigma}_{ij} + \tau_{ij})] \tag{3}$$

where $\bar{\sigma}_{ij}$ and τ_{ij} are the Favre-filtered viscous stress tensor and subgrid-scale viscous stress tensor, respectively. These are here defined as

$$\bar{\sigma}_{ij} = \mu\left(2\tilde{S}_{ij} - \tfrac{2}{3}\tilde{S}_{\mathrm{mm}}\delta_{ij}\right) \tag{4}$$

$$\tau_{ij} = \mu_t\left(2\tilde{S}_{ij} - \tfrac{2}{3}\tilde{S}_{\mathrm{mm}}\delta_{ij}\right) - \tfrac{2}{3}\bar{\rho}k^{\mathrm{SGS}}\delta_{ij} \tag{5}$$

where k^{SGS} is the subgrid-scale kinetic energy

$$k^{\mathrm{SGS}} = C_I\Delta^2\tilde{S}_{\mathrm{mn}}\tilde{S}_{\mathrm{mn}} \tag{6}$$

μ_t is the subgrid-scale dynamic viscosity

$$\mu_t = C_R\bar{\rho}\Delta^2\sqrt{\tilde{S}_{\mathrm{mn}}\tilde{S}_{\mathrm{mn}}} \tag{7}$$

and $\tilde{S}_{ij}$ is the Favre-filtered strain rate tensor given by

$$\tilde{S}_{ij} = \frac{1}{2}\left(\frac{\partial \tilde{u}_i}{\partial x_j} + \frac{\partial \tilde{u}_j}{\partial x_i}\right) \tag{8}$$

The subgrid heat flux appearing in the Favre-filtered energy equation is modeled using a temperature gradient approach

$$q_j = C_p\frac{\mu_t}{Pr_t}\frac{\partial \tilde{T}}{\partial x_j} \tag{9}$$

The filter width used in Eqs. (6) and (7) is the local grid cell width, that is, $\Delta = (\Delta_1\Delta_2\Delta_3)^{1/3}$. The subgrid-scale model used in this work is the Smagorinsky part of the model proposed by Erlebacher et al.[20] for compressible flows. The constants C_R and C_I appearing in Eqs. (6) and (7) are the Smagorinsky model constants. These are here given by

$$C_R = 0.012 \qquad C_I = 0.0066 \tag{10}$$

The system of governing equations, Eqs. (1–3), is closed by making assumptions concerning the thermodynamics of the gas considered. It is assumed that the gas is thermally perfect, that is, it obeys the gas law. Furthermore, the gas is assumed to be calorically perfect, which implies that internal energy and enthalpy are linear functions of temperature.

IV. Sound Propagation

Kirchhoff integration is a method for predicting the value of a property Φ, governed by the wave equation, at a point outside a surface enclosing all generating structures.[21] The method was originally used in the theory of diffraction of light and in other problems of an electromagnetic nature but has recently been used extensively for aeroacoustic applications. The integral relation is given by

$$\Phi(\boldsymbol{y}, t) = \frac{1}{4\pi}\int_S\left[\frac{\Phi}{r^2}\frac{\partial r}{\partial n} - \frac{1}{r}\frac{\partial \Phi}{\partial n} + \frac{1}{c_\infty r}\frac{\partial r}{\partial n}\frac{\partial \Phi}{\partial t}\right]_{\tau_r} \mathrm{d}S(\boldsymbol{x}) \tag{11}$$

where $\boldsymbol{y}$ is a observer location in the far field and $\boldsymbol{x}$ a location on the surface. The τ_r denotes that the expression within brackets is to be evaluated at retarded time, that is, emission time, and τ_r is related to the observer evaluation time t by the distance from the surface to the observer, $r = |\boldsymbol{y} - \boldsymbol{x}|$, and the speed of sound in the far-field region c_∞ as

$$\tau_r = t - r/c_\infty \tag{12}$$

The variable Φ to be evaluated is in this case the surface pressure. S denotes the surface enclosing all sound-generating structures and n denotes the surface normal, positive outward. The surface S must be placed in a region where the flow is completely governed by a homogeneous linear wave equation with constant coefficients.[6] More detail on the Kirchhoff surface integration method can be found in, for example, Freund et al.[6] and Lyrintzis.[21]

The strength of the sources in the hydrodynamic jet region decays slowly downstream, which means that the downstream end of a closed surface will enter regions of considerable hydrodynamic fluctuations (see Fig. 1). It is thus common practice to use Kirchhoff surfaces that are not closed in the upstream and downstream ends. It was shown by Freund et al.[6] that the errors introduced by using such surfaces are small if the main portion of the sound sources are within the axial extent of the surface and if lines connecting observer locations with locations in the hydrodynamic region, representing

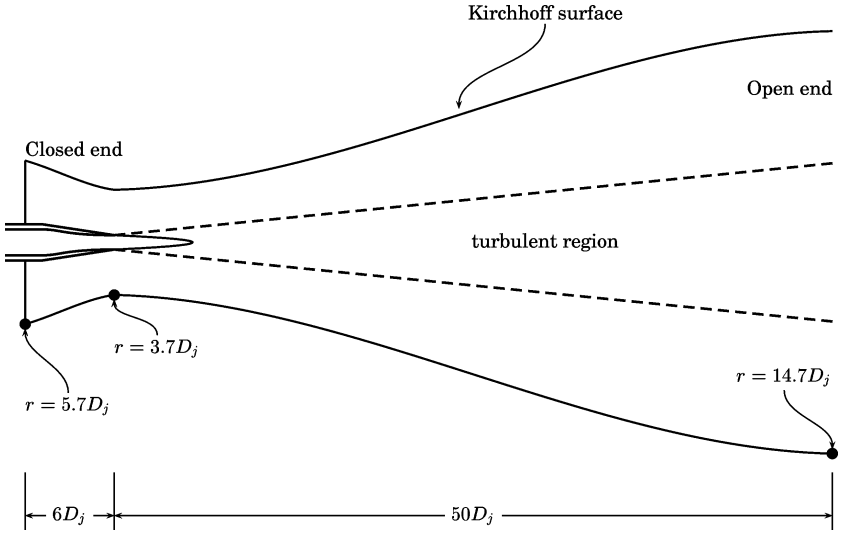

Fig. 1 Jet-fitted Kirchhoff surface closed in the upstream end and open in the downstream end.

the main sources of sound, intersect with the surface. Rahier et al.[22] found that the downstream closing surface only gives a minor contribution to the radiated sound. In the work presented in this paper, a Kirchhoff surface closed in the upstream end and open in the downstream end was used (see Fig. 1).

One of the main strengths of the Kirchhoff surface integral approach, contrary to many other methods, is the fact that as long as all sources of sound, flow inhomogeneities, and objects that in some way affect the radiated sound are bounded by the surface, all of these effects are included. This, for example, means that no extra treatment has to be considered to be able to predict the effects of refraction and convection.

V. Method

A. Numerical Scheme

The Favre-filtered Navier–Stokes equations were solved using a finite volume method solver with a third-order low-dissipation upwind scheme for the convective fluxes and a centered difference approach for the diffusive fluxes. The temporal derivatives were estimated using a second-order three-stage Runge–Kutta technique. The solver used is based on the G3D family of codes developed by Eriksson.[23] The convective scheme is a combination of centered and upwind-biased components that have been used with good results for free shear flows by Mårtenson et al.[24] and, more recently, for shock/shear-layer interaction by Wollblad et al.[25] The coefficients of the low-dissipation upwind scheme used for estimating the convective flux over a cell face are derived using a third-order polynomial $Q(x)$ to represent the variation of the flow state in the direction normal to the face (see Fig. 2).

$$Q(x) = A + Bx + Cx^2 + Dx^3 \tag{13}$$

The face state is evaluated using the interpolated value $Q(0)$, modified to include upwinding by adding the third derivative of $Q(x)$ according to

$$Q_0 = Q(0) + \delta \frac{\partial^3 Q}{\partial x^3}(0) = A + 6\delta D$$

$$= C_1\bar{Q}_1 + C_2\bar{Q}_2 + C_3\bar{Q}_3 + C_4\bar{Q}_4 \tag{14}$$

where the coefficient δ in front of the upwind term has been chosen by numerical experiment[24] to be 1/96 to introduce only a small amount of upwinding. The result is the low-dissipation third-order upwind scheme used in this work, that is, low dissipation compared to a standard third-order upwind scheme, which is obtained using $\delta = 1/12$. The coefficients ($C1$–$C4$) of the low-dissipation third-order upwind scheme are

$$C_1 = -(1/12 + \delta) = -9/96 \qquad C_2 = (7/12 + 3\delta) = 59/96$$

$$C_3 = (7/12 - 3\delta) = 53/96 \qquad C_4 = -(1/12 - \delta) = -7/96 \tag{15}$$

For more detail on the numerical scheme, see Eriksson.[23] One-dimensional convection can be described by the following relation:

$$\frac{\partial u}{\partial t} + c\frac{\partial u}{\partial x} = 0 \tag{16}$$

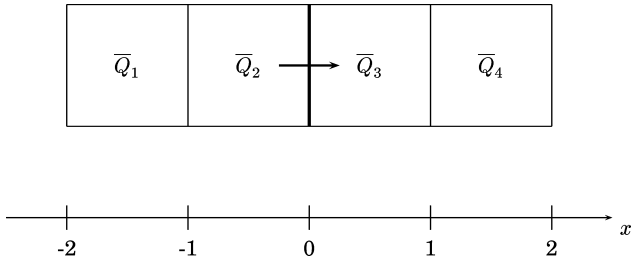

Fig. 2 Face states estimated from the cell-averaged state in four neighboring cells.

where c is a constant coefficient. Assuming an initial solution to Eq. (16) of harmonic type, its exact solution can be written as

$$u(x, t) = u_0 \exp(st) \exp(-ikx) \tag{17}$$

where u_0 is a constant amplitude and k is the wave number. The time-dependent part of the solution is $\exp(st)$ and s describes its time dependence. Inserting Eq. (17) in Eq. (16) gives $s = ikc$, which implies that the exact solution to Eq. (16) will have a periodic behavior in time without damping or amplification. Furthermore, the phase velocity will be the same for all wave numbers, namely, the constant c.

An even-order central numerical approximation to a first-order derivative does not introduce any numerical dissipation in itself. Therefore, dissipation is often added in the range of wave numbers for which the dispersion errors are significant. Artificial numerical dissipation is introduced by adding an even-order derivative, which corresponds to adding $(-1)^{n+1}\delta(\partial^{2n}u/\partial x^{2n})$ on the right-hand side of Eq. (16). Discretizing Eq. (16) using a finite volume method approach implies that first-order derivatives are estimated by differences of cell face averages. Because the cell-face-averaged properties, in the solver used in the present work, are obtained using a third-order upwind scheme where the upwinding is established by adding a third-order derivative, this corresponds to a fourth-order centered scheme with a fourth-order derivative added to introduce dissipation, in finite difference terms. The time dependence s for the discretized case, using a five-point stencil, becomes

$$s = \frac{c}{\Delta x}\left\{ 2i \sum_{l=1}^{2} a_l^{\mathrm{FDM}} \sin(lk\Delta x) - \delta\left[d_0^{\mathrm{FDM}} + 2\sum_{l=1}^{2} d_l^{\mathrm{FDM}} \cos(lk\Delta x) \right] \right\} \tag{18}$$

where a_l^{FDM} corresponds to the finite difference coefficients defining the central scheme and d_l^{FDM} the finite difference coefficients defining the derivative added for upwinding. The amount of dissipation added is prescribed by the constant δ. Figure 3 shows the dispersion relation and dissipation relation of the scheme used in the present work. The dispersion relation is the imaginary part of Eq. (18), and the dissipation relation is the real part. For comparison the dispersion relation of the fourth-order dispersion-relation-preserving scheme proposed by Tam and Webb[26] is included in Fig. 3a. The time-stepping scheme will modify the dispersion and dissipation errors, but for the Courant–Friedrichs–Lewy (CFL) number chosen in the present study CFL ≤ 0.5 the effects are small (see Billson[27]).

B. Computational Setup

Figure 4 gives an overview of the computational domain used for the LES. In this figure, the upper half of the three-dimensional domain used for the calculations is shown. To minimize the effect of reflections at the domain outlet on the predicted flowfield, a damping zone was added at the domain outlet. The functionality of this damping zone or buffer layer has been described in more detail in Andersson et al.[28] and Andersson.[29] The axial extent of the physical part of the domain downstream of the nozzle exit is 2.5 m, which is equal to 50 nozzle diameters ($D_j = 50$ mm). The radial extent is $10D_j$ at the nozzle-exit plane and $20D_j$ at the domain outlet. The physical part of the computational domain was discretized using a block-structured boundary-fitted mesh with 33 mesh blocks and approximately 3×10^6 cells (see Figs. 5a and 5b). Additionally 5×10^5 cells were used to discretize the damping zone. To avoid a centerline singularity and to establish mesh homogeneity through out the domain, a combination of polar and Cartesian blocks was used (see Fig. 5b). The grid cells are stretched in the downstream direction and radially toward the boundaries using cubic Hermite grid point distribution.

For all free boundaries, that is, the upstream and entrainment boundaries, absorbing boundary conditions based on the method of

characteristics were adopted. Static pressure was specified at the domain outlet, that is, at the downstream end of the buffer layer, and at the nozzle inlet P_0 and h_0 were specified. No unsteady forcing of incoming disturbances at the domain inlet was utilized to trigger the initial development of the jet. The velocities specified at the entrainment boundaries were interpolated from corresponding Reynolds-averaged Navier–Stokes (RANS) calculations. The calculation domain used for these RANS computations is sufficiently large to ensure that no disturbances caused by the outlet boundaries will reach the location of the LES domain boundaries. Figure 6 shows a comparison of the LES and RANS calculation domains.

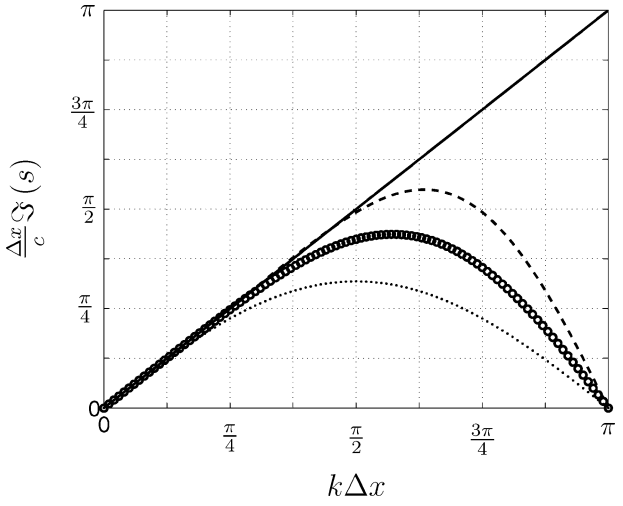

a) Dispersion relation

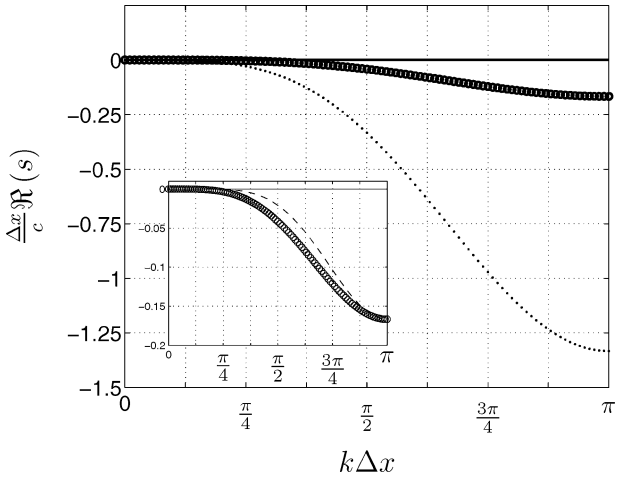

b) Dissipation relation

Fig. 3 Dispersion and dissipation relations: ○, numerical scheme used in the present work; and ——, denote the exact solution: a) – – –, fourth-order DRP scheme proposed by Tam and Webb[26] and · · · ·, dispersion relation for a second-order centered scheme; and b) ○, dissipation relation for a fourth-order derivative with an amplifying factor $\delta = 1/96$ and · · · ·, same fourth-order derivative with $\delta = 1/12$, that is, the standard third-order upwind scheme. The enclosed figure shows a comparison of dissipation relations for a fourth-order derivative (○) and a sixth-order derivative (– – –).

VI. Results

This section gives predictions of near-field aerodynamics of a Mach 0.75 jet and its radiated sound. The calculations were started up using initial solutions interpolated from two-dimensional axisymmetric RANS calculations. For jet 1, the simulation ran for

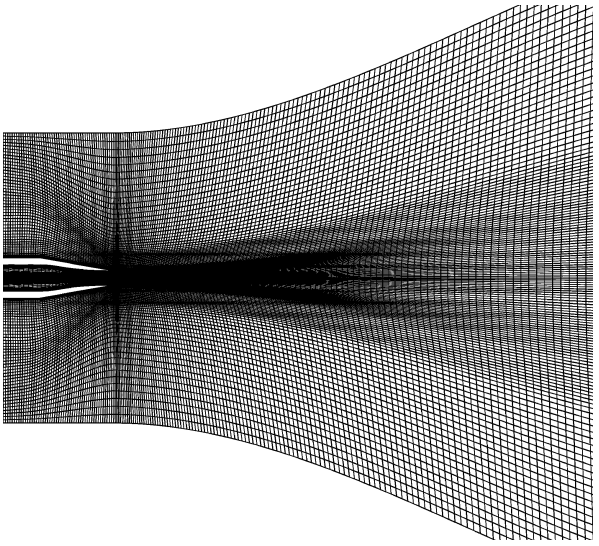

Fig. 5a Slice through the calculation domain made at $z = 0$, that is, a *xy* plane. The figure shows the domain inlet including the nozzle and the outer boundaries in the radial direction. The axial extent of the computational domain is roughly twice that shown.

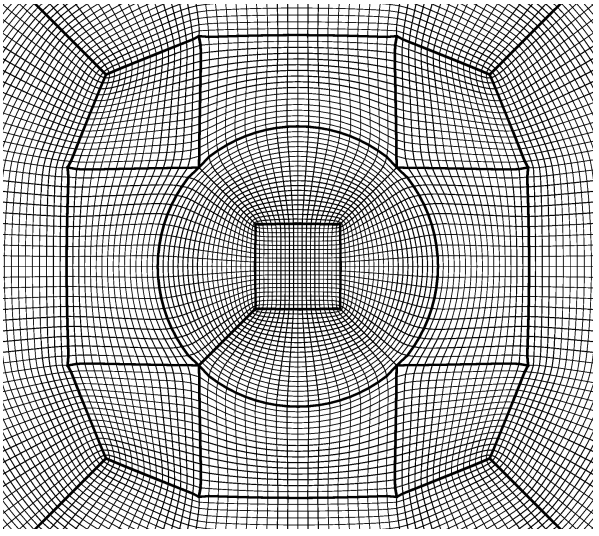

Fig. 5b Slice through the calculation domain at constant *x*, that is, a *yz* plane. Combining Cartesian and polar grid blocks enhances the radial direction grid homogeneity throughout the domain.

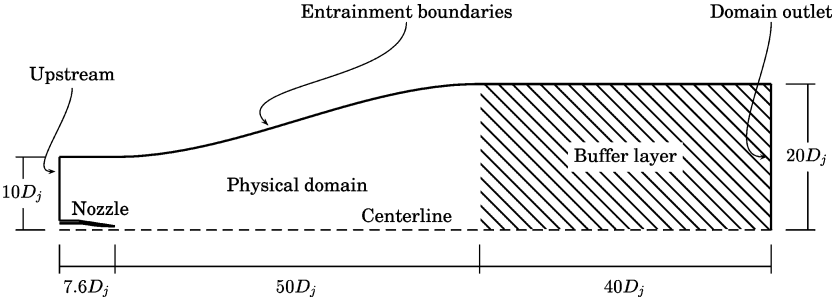

Fig. 4 Computational setup.

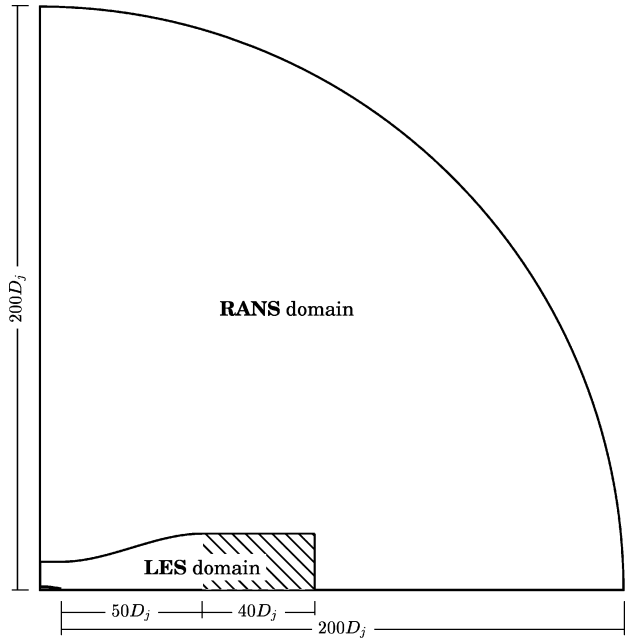

Fig. 6 Entrainment velocities were obtained from RANS calculations performed using a significantly larger domain.

about 1.0×10^5 time steps ($\Delta t = 0.25\ \mu$s) before sampling was initiated. This corresponds to 0.025 s of simulated time or roughly 3.5 acoustic through-flows, that is, the time required for an acoustic wave to travel through the calculation domain, not including the outlet buffer layer, based on the speed of sound at ambient conditions. Sampling of statistical data was then continued for another 20 acoustic through-flows. Each acoustic through-flow corresponds to roughly 32 h of computer wall time using 14 AMD 1700^+ processors of our Linux cluster. For jet 2, as for jet 1, about 3.5 acoustic through-flows were completed before sampling of data was initiated, which in this case corresponds to roughly 1.7×10^5 time steps ($\Delta t = 0.15\ \mu$s). Sampling of statistical data was then continued for about 14 acoustic through-flows. In this case, because of the shorter time step, each acoustic through-flow corresponds to roughly 54 h of computer wall time. The time steps were chosen such that the CFL number was not larger than 0.5 anywhere. Profiles of statistical quantities to be presented in the following sections are obtained from flowfield data that were averaged in both time and the azimuthal direction to establish improved statistical convergence. The profiles are made nondimensional using the jet velocity at the nozzle exit U_j and the nozzle outlet diameter D_j. More detail on the results presented in this section can be found in Andersson[29] and Andersson et al.[28]

A. Instantaneous and Time-Averaged Flowfield

Figure 7 depicts contours of instantaneous axial velocity in a plane along the jet axis, $y = 0$. Comparing the contours in Fig. 7a, which represent jet 1, with those obtained for jet 2 (Fig. 7b), it seems that heating the jet results in a higher initial mixing and hence a shorter potential core region. Furthermore, the heated jet seems to be narrower than the isothermal jet. According to Hinze,[30] experiments have indicated that increasing the temperature ratio T_j/T_∞ gives a narrower jet. Furthermore, it has been observed that the length of the potential core decreases with increased temperature ratio.[30] Figure 8 shows contours of instantaneous axial velocity in a plane cutting through the jet at $x = 3.0D_j$. These figures clearly visualize the asymmetric nature of the jet at an instant in time.

Profiles of mean-flow quantities were extracted along the centerline and along radial lines at three axial positions downstream of the nozzle exit according to Fig. 9. Although the time-averaged flowfield is generally in good agreement with the measured quantities, there are some discrepancies. In the predicted flowfield the initial mixing is overpredicted, resulting in a shorter potential core region. Figure 10 gives a comparison of predicted and measured centerline

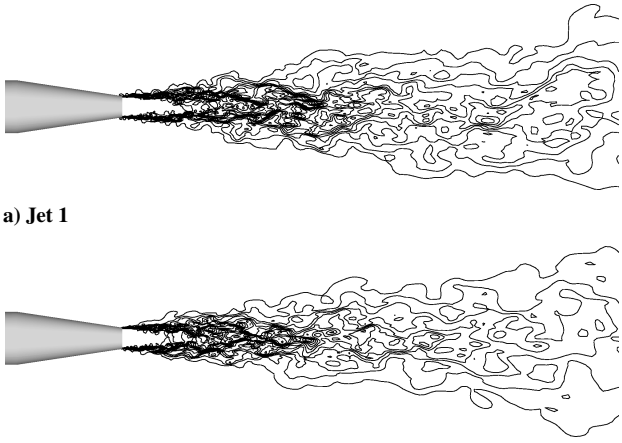

a) Jet 1

b) Jet 2

Fig. 7 Contours of instantaneous axial velocity ($y = 0$).

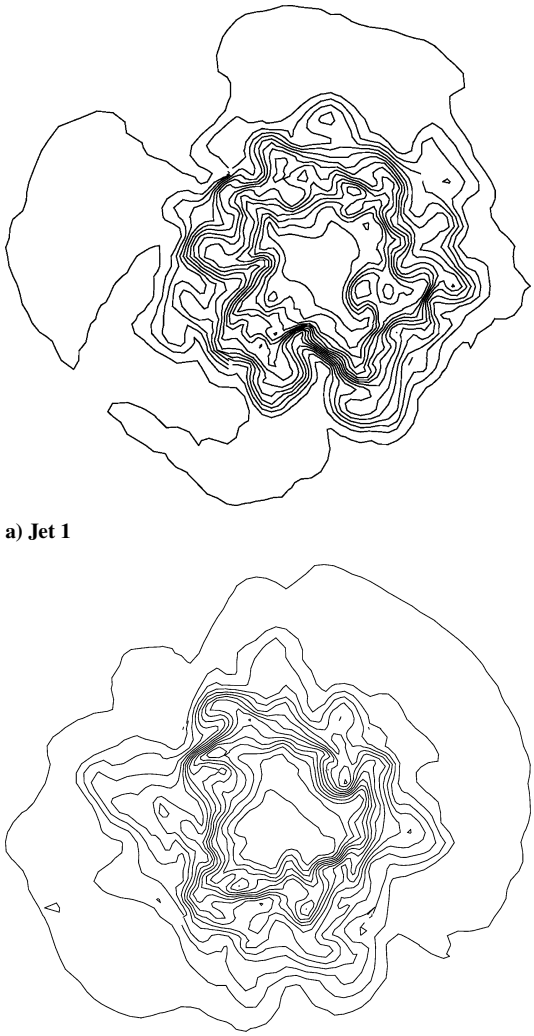

a) Jet 1

b) Jet 2

Fig. 8 Contours of instantaneous axial velocity ($x = 3.0D_j$).

axial velocity for the two jets. Defining the length of the potential core L_c as the axial location where the averaged axial velocity is 0.95 U_j gives for jet 1 $L_c = 5.5D_j$ and for jet 2 $L_c = 4.0D_j$, which should be compared with $L_c = 6.5D_j$ and $5.0D_j$ for the experimental data.

Figure 11 shows radial profiles of axial velocity. Figure 12 gives a comparison of turbulence intensities. The differences in levels of u'_{rms} and v'_{rms} indicate that the turbulence anisotropy is captured. The peak levels of predicted turbulence intensity are shifted toward the nozzle exit, which is consistent with the underprediction of potential

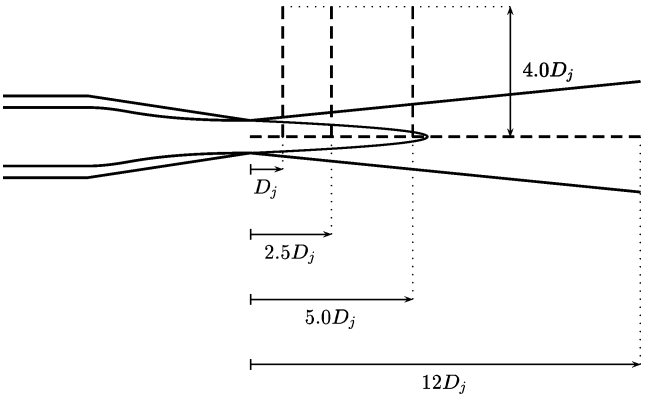

Fig. 9 Lines along which profiles of time-averaged quantities were extracted are denoted by dashed lines.

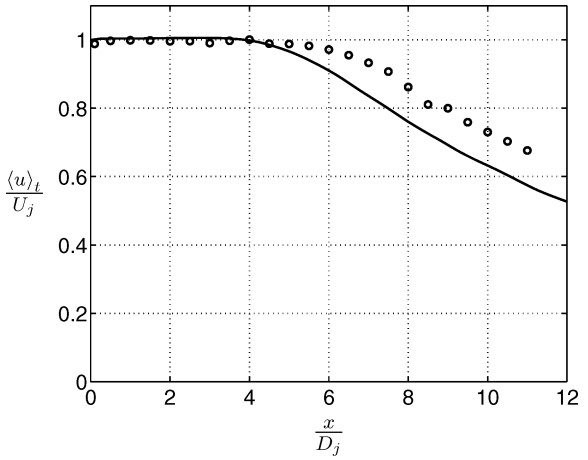

a) Jet 1

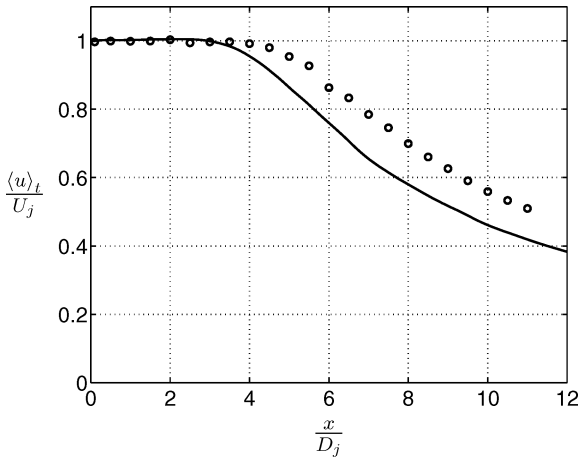

b) Jet 2

Fig. 10 Centerline profile of time-averaged axial velocity: ——, LES and ○, measurements.[16]

core lengths because the maximum turbulence intensity is found where the potential core closes. Figure 13 shows radial profiles of $u'v'$ correlations. The maximum correlation levels are overpredicted near the nozzle exit, which again is consistent with the higher degree of mixing found in the LES data.

The reason for the underprediction of the length of the potential core region can probably be found in a combination of several factors. The most important are probably subgrid-scale viscosity, numerical scheme, inflow conditions, and entrainment boundary conditions. The large $u'v'$ in the predicted initial jet region indicates that a transition takes place in the shear layer near the nozzle lip (see

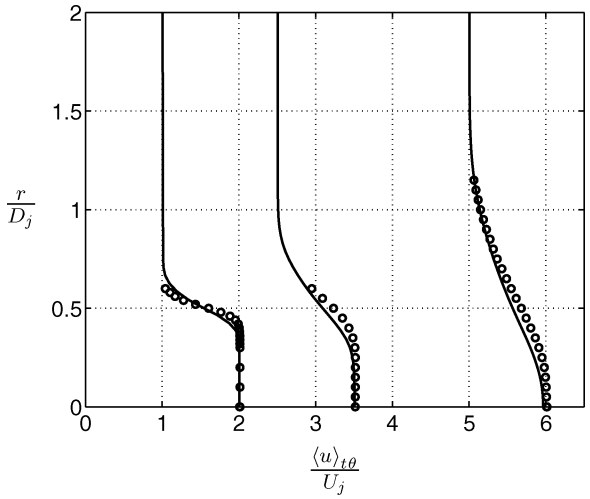

a) Jet 1

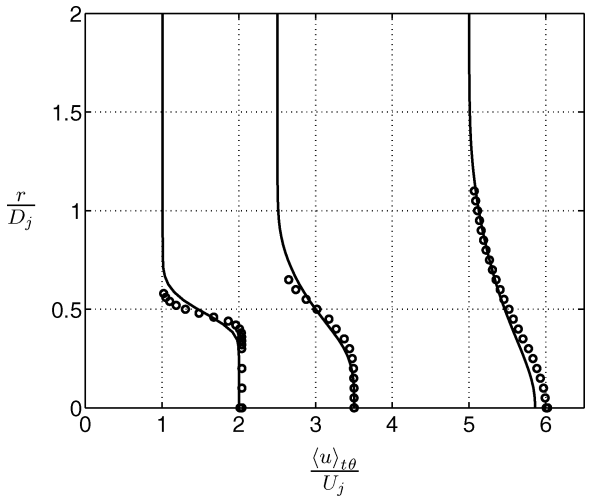

b) Jet 2

Fig. 11 Radial profiles of axial velocity. The profiles have been staggered according to their axial location. See also legend to Fig. 10.

Fig. 13). The fact that the predicted $u'v'$ correlations for locations farther downstream are closer to the measured correlations and that the maximum turbulence intensities are captured by the LES (see Fig. 12), shows that once the transition process is completed the flow is physically correct. However, the overpredicted mixing caused by the initial transition seems to result in a shorter potential region. An increase in the subgrid-scale dissipation would probably decrease the turbulence intensity and delay the transition process and thus change the length of the potential core. Depending on the amount of dissipation, the potential core length could either be shortened or elongated. The effect of an increase of artificial dissipation introduced by the numerical scheme is likely to be similar to that of increased subgrid-scale dissipation.

Bogey and Bailly[10] investigated the effects of the inflow conditions on the jet flow. It was found that the use of a smaller shear-layer momentum thickness resulted in higher turbulence intensities in the shear layer and hence a more rapid transition. In the present study a thinner boundary layer on the nozzle walls would probably imply less overpredicted initial mixing that might affect the length of the potential core. Adding unsteady forcing of incoming disturbances at the domain inlet could possibly affect the transition process and weaken the initial mixing.

Concerning the effects of the entrainment flow, only the correct entrained mass flow will give the correct flow behavior in the hydrodynamic region. Lack of entrained mass will be compensated by backflow, which results in a recirculation zone surrounding the jet and prevents it from spreading correctly. However, the RANS

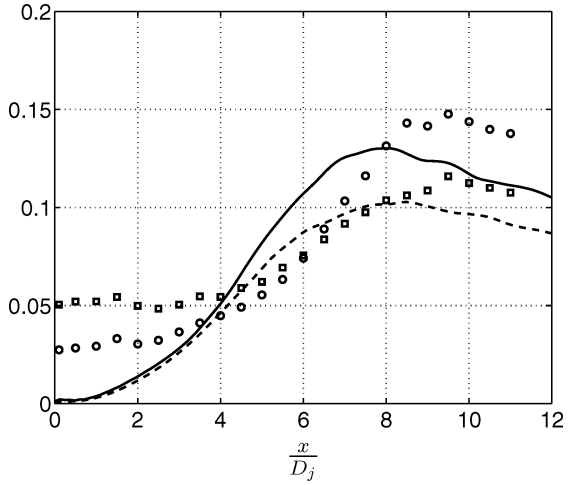

a) Jet 1

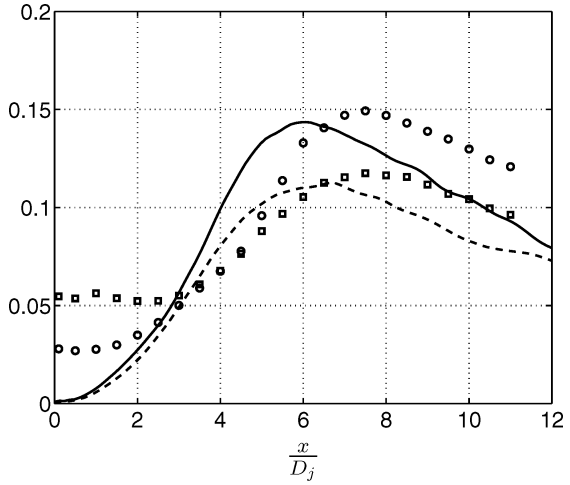

b) Jet 2

Fig. 12 Axial profiles of turbulence intensities: —— and – – –, u'_{rms} and v'_{rms}, respectively; and ○ and □, corresponding measured[16] quantities.

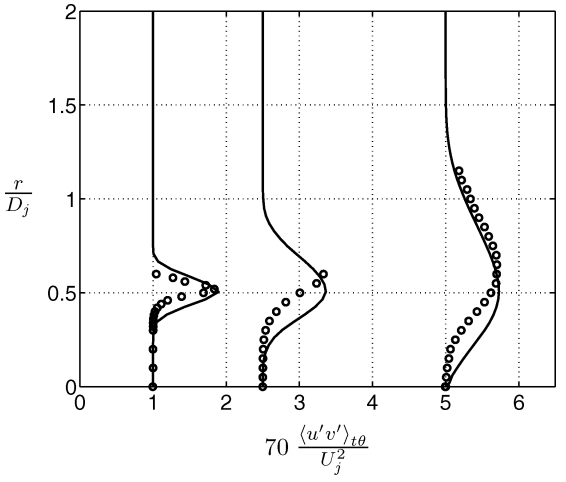

a) Jet 1

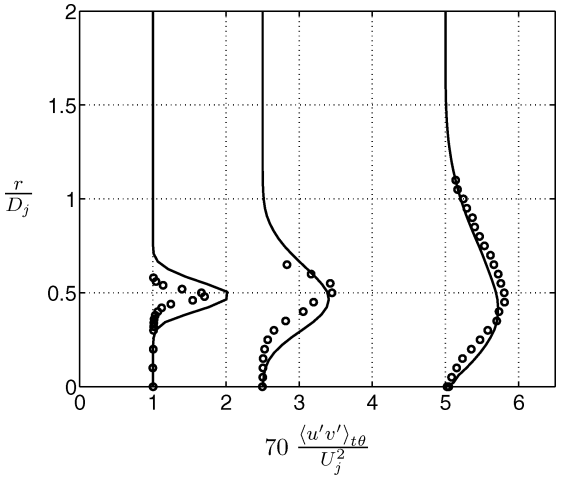

b) Jet 2

Fig. 13 Radial profiles of predicted and measured $u'v'$ correlation (see also legend to Fig. 10).

computations from which the boundary entrainment velocities have been interpolated give a somewhat overpredicted potential core length. In summary, the correct potential core length can probably be obtained by modification of the subgrid-scale properties alone. However, a more physical approach would be to modify the inflow conditions to produce results in better agreement with measurements.

B. Two-Point Space–Time Correlations

Two-point space–time correlations were obtained for the axial-velocity component in a few shear-layer locations along the nozzle lip line. The two-point space–time correlation of axial velocity for a certain spatial separation ξ and separation in time τ is given by

$$\mathcal{R}_{uu}(\boldsymbol{x},\xi,\tau)=\frac{\langle u'(\boldsymbol{x},t)u'(\boldsymbol{x}+\xi,t+\tau)\rangle_t}{\sqrt{\langle u'^2(\boldsymbol{x})\rangle_t}\sqrt{\langle u'^2(\boldsymbol{x}+\xi)\rangle_t}} \tag{19}$$

where u' denotes resolved fluctuation of axial velocity and $\boldsymbol{x}$ is the position in the flowfield where the two-point correlation is evaluated. Figure 14 shows correlations obtained in the shear layer at an axial location corresponding to the potential core closure. The curve centered at $\tau=0$ corresponds to the autocorrelation and each consecutive curve is obtained by increasing the spatial separation ξ by $0.3D_j$. For homogeneous isotropic turbulence the correlation peak would be unity for all spatial separations, that is, the increasing deviation from unity with increasing spatial separation is a measure of how far from frozen the turbulence is. The shape of the correlation curves as well as the correlation envelope, that is, the curve connecting the correlation peaks, is in rather good agreement with the measured data. Figure 15 depicts contours of two-point space–time correlations in the $\xi\tau$ plane. Again, the correlations have been obtained in the shear layer at the end of the potential core. The peaks of the predicted correlations are indicated by stars, and those of the correlations obtained from the two-point measurements (Refs. 18 and 19; P. Jordan, private communication, 2003) are indicated by circles. The slope of a line connecting the correlation peaks corresponds to the local convection velocity of turbulence structures.

Figure 16 gives a comparison of predicted correlations for jets 1 and 2. The correlations are presented in the shear layer at axial positions normalized with the length of the potential core. As can be seen, there are no great differences in the correlations for the two jets. However, because the potential core is shorter for jet 2, turbulence scales grow faster for this jet.

C. Length and Timescales of Turbulence Structures

Estimates of local integral length and timescales of turbulence structures were obtained by integration of the corresponding autocorrelation and spatial correlation, respectively. The first crossing of the coordinate axis was used as the upper limit for the integration. Figure 17 gives a comparison of length and timescales for jets 1 and 2. In Fig. 17a, the axial development of predicted integral length scale is depicted. To be able to make a comparison of the two jets, the axial coordinate has been normalized by the length of the potential core. Figure 17b shows the axial development of integral timescale. Scales obtained from the two-point measurements (Refs. 18 and 19; Jordan, private communication) are indicated by circles and stars for jets 1 and 2, respectively.

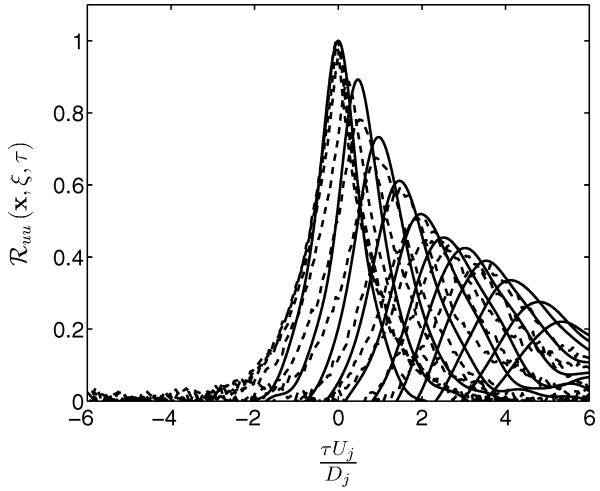

a) Jet 1

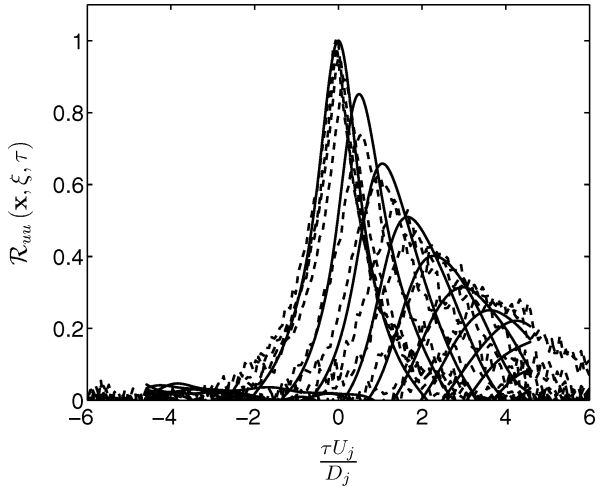

b) Jet 2

Fig. 14 Two-point space–time correlations obtained in the shear layer at the end of the potential core ($x = L_c$, $r = 0.5D_j$): ——, LES data and – – –, measurements (Refs. 18 and 19; Jordan, private communication).

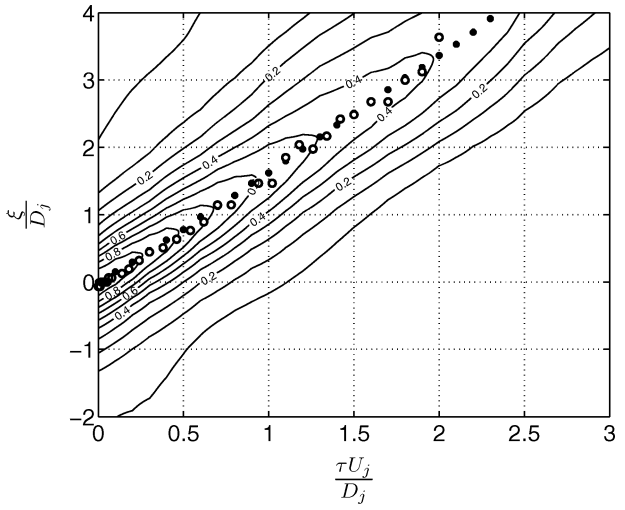

a) Jet 1

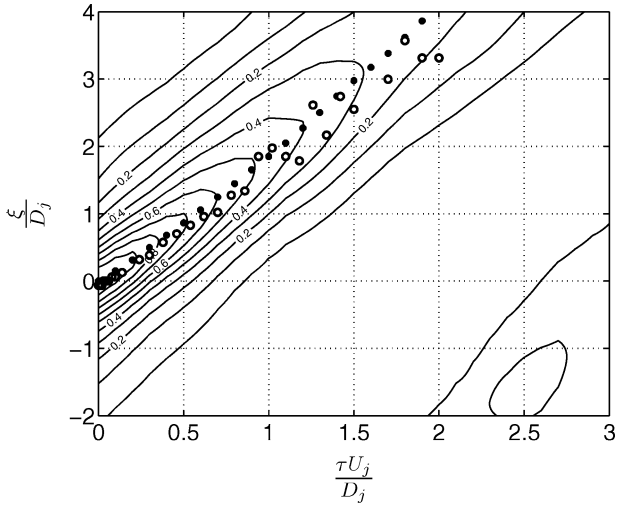

b) Jet 2

Fig. 15 Contours of two-point space–time correlations obtained in the shear layer at the end of the potential core ($x = L_c$, $r = 0.5D_j$). The peaks of the predicted correlations are indicated by stars, and the peaks of the measured data (Refs. 18 and 19; Jordan, private communication) are indicated by circles.

D. Far-Field Sound Pressure Levels

Power spectra of pressure fluctuations and sound pressure levels have been obtained for a few far-field observer locations. The observer locations coincide with the microphones in the experimental setup[17] (Fig. 18). The sound pressure level is here defined as

$$\mathrm{SPL} = 20\log_{10}\left[\sqrt{\langle (p')^2\rangle_t}\Big/ p_{\mathrm{ref}}\right] \tag{20}$$

where

$$p_{\mathrm{ref}} = \sqrt{\rho_\infty c_\infty 10^{-12}} = 2.0 \times 10^{-5}\ \mathrm{Pa} \tag{21}$$

Figure 19 shows a comparison of predicted and measured[17] power spectra for a few observer locations on the inner arc ($r = 30D_j$). To make the comparison with measured data easier, the spectra have been filtered in third octave bands. The spectra have been staggered by multiplying the intensity by a factor $C = 10^{2n}$, where $n = [(\theta - 20)/40]$, θ being the angle from the jet axis (Fig. 18). This amplification corresponds to a $20n$-dB shift of the spectra. The sound pressure level as function of frequency is obtained as

$$\mathrm{SPL}(f) = 20\log_{10}\left[\sqrt{(C\,\widehat{p'}\widehat{p'}^{*})}\Big/ p_{\mathrm{ref}}\right] \tag{22}$$

where $\widehat{p'}$ denotes the Fourier transform of the pressure fluctuation and $\widehat{p'}^{*}$ its conjugate. The oscillating nature of the spectra in the low-frequency range is because the length of the time series used is insufficient to fully resolve these low frequencies. For low and high angles, the predicted levels are in good agreement with the experimental data up to at least Strouhal number = 1.5 (see Fig. 19). For the intermediate angles on the other hand, the predicted amplitude decreases rapidly above $Sr = 1.0$. This is because the grid is not fine enough to support high-frequency acoustic waves in the radial direction. Assuming that it is sufficient to have four cells per wavelength to be able to capture a propagating wave of a certain frequency, the cells in the area where the Kirchhoff surface is located would support propagating waves of Strouhal numbers up to $Sr \simeq 1.2$. This means that the mesh itself acts as a low-pass filter as the acoustic waves propagate through the domain. This effect is especially noticeable for the intermediate angles, where the mesh, caused by the resolution demands at the jet exit, is very coarse (see Fig. 5a). The filtering of acoustic waves caused by the coarseness of the mesh might be an explanation for the somewhat overpredicted spectrum amplitudes in the high-frequency range for the observers on the forward arc ($\theta > 90$ deg) (see Fig. 19). This overprediction might be caused by unphysical, high-frequency acoustic waves generated in the hydrodynamic jet region. An indication of such pollution of high frequencies by the presence of spurious noise was found when Lighthill's[9] acoustic analogy was used for sound propagation, which has been reported in Andersson.[29] These high-frequency waves will, for most observers, be damped out by numerical dissipation. However, in the upstream direction the resolution is significantly finer relative to the downstream direction, which means that some of these

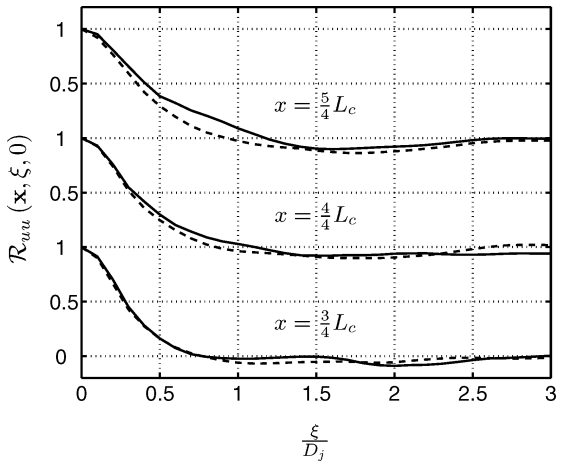

a) Spatial correlations

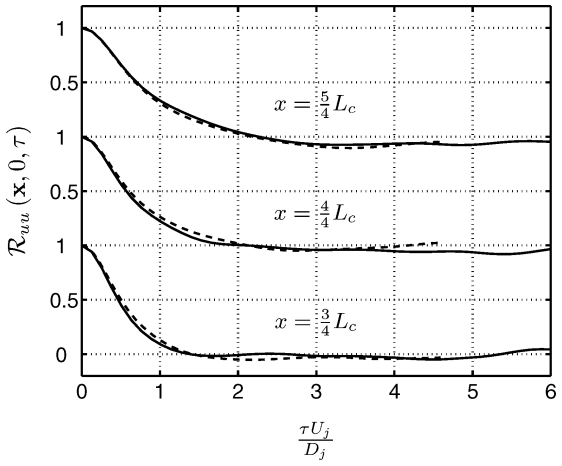

b) Autocorrelations

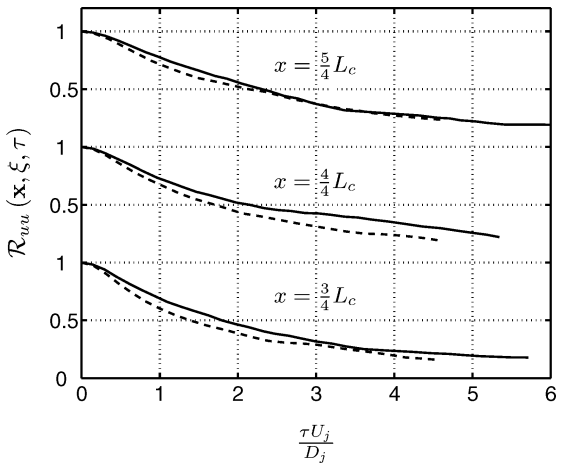

c) Correlation envelopes

Fig. 16 Comparison of predicted spatial correlations, autocorrelations, and space–time correlation envelope for ——, jet 1 and – – –, jet 2.

nonphysical waves might reach the Kirchhoff surface and thus contribute to the predicted pressure signal. Figure 20 gives a comparison of predicted and measured SPL for the inner arc. The predicted SPL have been obtained by integration of the corresponding spectra excluding the contribution from frequencies lower than Strouhal number $Sr = 0.05$. The underprediction of the spectrum amplitude above $Sr = 1.0$ gives underpredicted SPL for the observers between 50 and 120 deg for jet 1. This effect does not show up in the sound pressure levels for jet 2 though. For jet 2 SPL for the 20-deg observer is underpredicted, which also can be seen in the power spectrum for

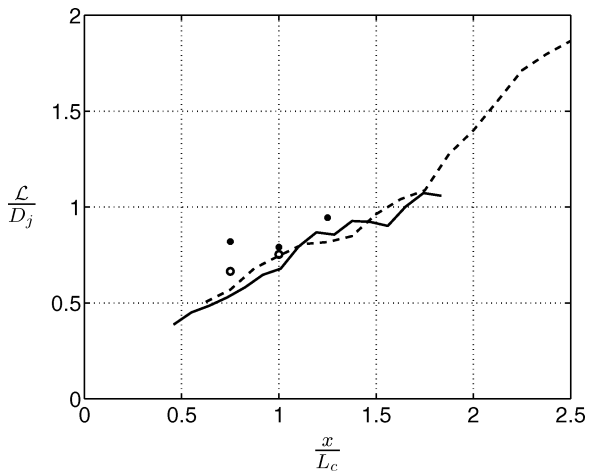

a) Integral length scale $\mathcal{L}$

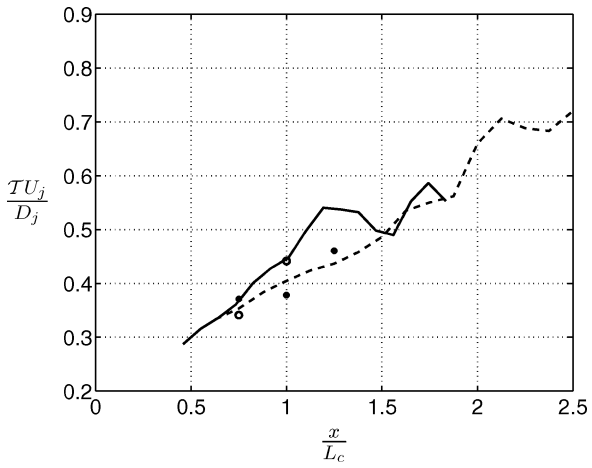

b) Integral timescale $\mathcal{T}$

Fig. 17 Axial development of integral length and timescale: ——, jet 1; – – –, jet 2; ○ and □, corresponding measured (Refs. 18 and 19; Jordan, private communication) quantities.

this observer location where the peak level is underpredicted. As can be seen in Fig. 18, the 20-deg observer is very close to the integration surface, which can affect the results. Figure 20 shows that the overall directivity is captured and that a peak in the radiated sound can be found for observers in the region of 20–30 deg from the axis.

Figures 21 and 22 show power spectra and sound pressure levels for the observers on the $50D_j$ arc, respectively. Figure 23 (Refs. 12, 17, and 31–33) gives a comparison of predicted SPL for jet 1 with various sets of measured data obtained for unheated jets. The measured acoustic intensities $I = p'p'$ have been scaled to $M_j = 0.75$ and $r/D_j = 30$ according to

$$I \sim U_j^8 D_j^2 \big/ c_\infty^5 r^2 \tag{23}$$

The predicted SPL shows a clear increase for observation angles greater than 110 deg unlike all of the experimental results represented in Fig. 23. As mentioned earlier, this behavior might be an effect of contamination of the near-field data in the upstream arc. Note that the measurements by Jordan et al.[17] deviate significantly from classical measurements by Mollo-Christensen et al.,[31] Lush,[32] and Tanna[12] near 90 deg; the predicted levels are, however, very close to the results by Jordan et al.[17]

There are not very large differences in the sound pressure levels obtained for jet 1 and those obtained for jet 2 (Fig. 24). According to Jiang et al.,[34] increasing the jet to ambient temperature ratio results in a weaker sound source but increased sound pressure levels. Tests done to investigate the heating effects on the radiated sound have shown that for high exhaust speeds increasing the jet to ambient

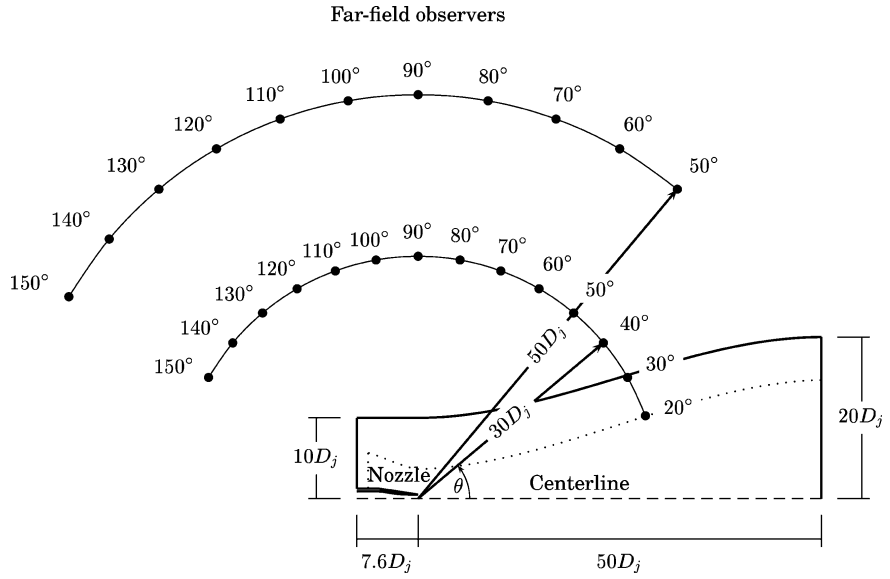

Fig. 18 Acoustic pressure fluctuations were evaluated in 25 observer locations situated on two arcs in the far-field regions of the jet: · · · ·, Kirchhoff surface.

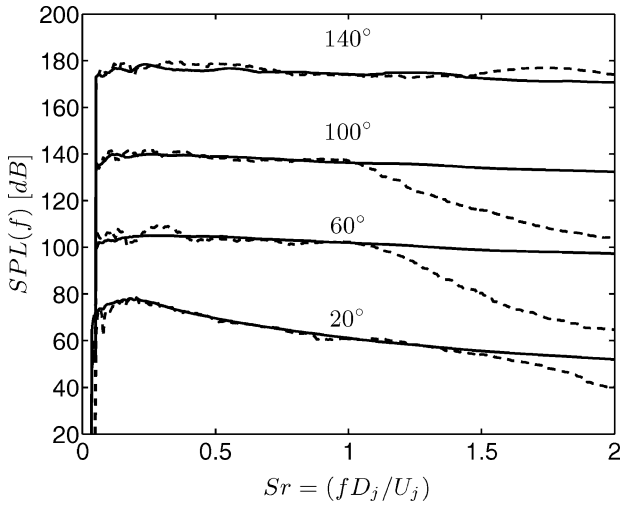

a) Jet 1

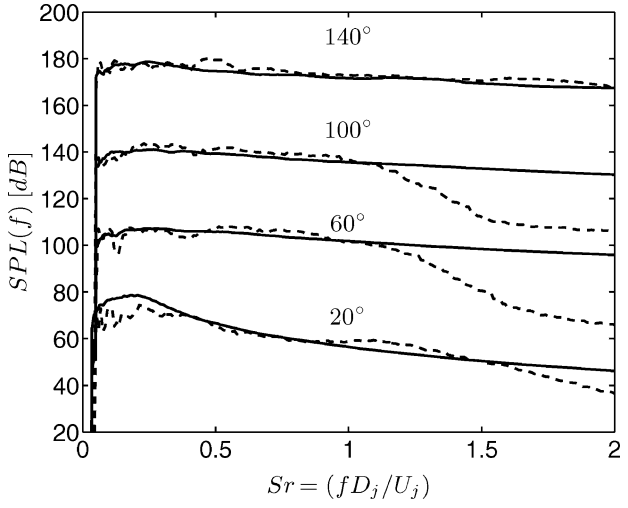

b) Jet 2

Fig. 19 Comparison of – – –, predicted and ——, measured[17] power spectra of far-field pressure signal for a few observer locations on the inner arc ($r = 30D_j$). The spectra have been staggered by adding a factor $20n$ [dB] where $n = [(\theta - 20)/40]$, θ being the angle from the jet axis.

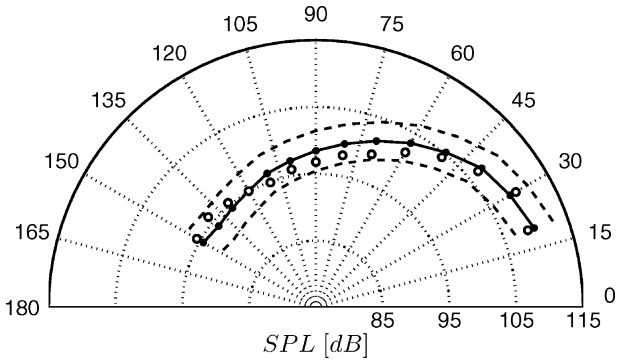

a) Jet 1

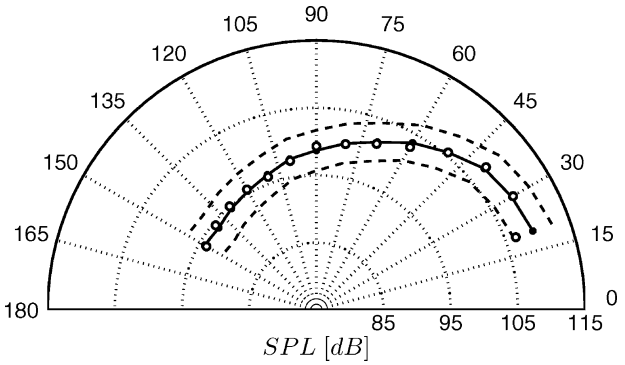

b) Jet 2

Fig. 20 Sound pressure levels in observer locations situated $30D_j$ from the nozzle outlet at different angles θ measured from the jet axis (see Fig. 18): ——, measured[17] levels and – – –, measured levels ±3.0 dB. Predicted SPL obtained using Kirchhoff surface integration are represented by ○.

temperature ratio reduces the noise levels, whereas at lower exhaust speeds the heated jet is the noisier.[35] The slight increase in SPL found for jet 2 is, however, not sufficiently large to be able to draw any conclusions regarding the heating effects on radiated sound in this study. Moreover, the measurements by Tanna,[12] where a wide range of exhaust velocities and temperature ratios were tested, indicates that Mach number 0.75 is in the range where the trend changes from increase to decrease of emitted sound as increasing the temperature ratio, and thus the heating effects on the sound pressure levels in the far field should be small at this Mach number. However, although the

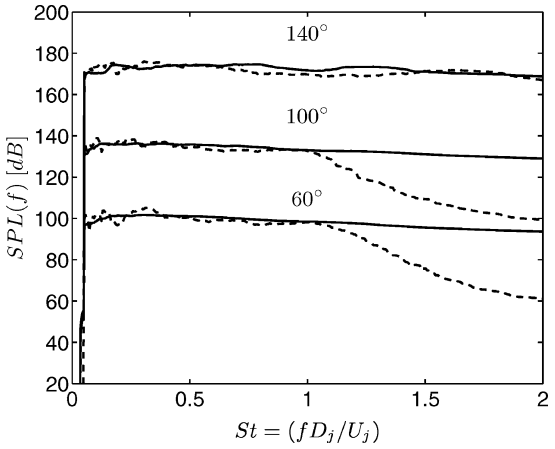

a) Jet 1

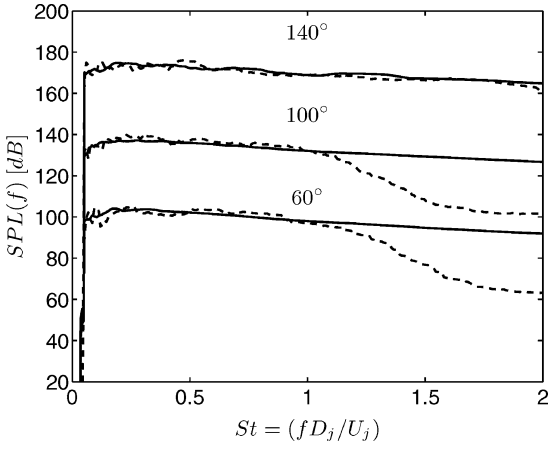

b) Jet 2

Fig. 21 Power spectra of far-field pressure signal for a few observer locations on the outer arc ($r = 50D_j$). See also legend to Fig. 19.

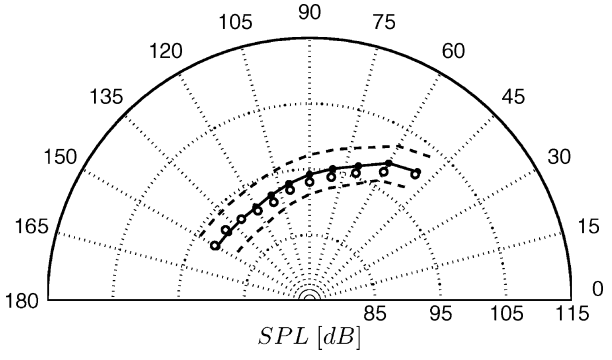

a) Jet 1

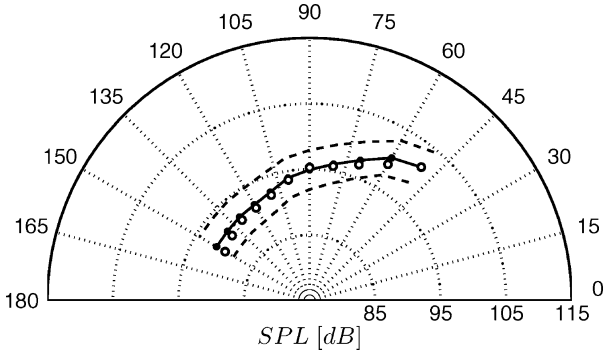

b) Jet 2

Fig. 22 Sound pressure levels in observer locations situated $50D_j$ from the nozzle outlet; see also legend to Fig. 20.

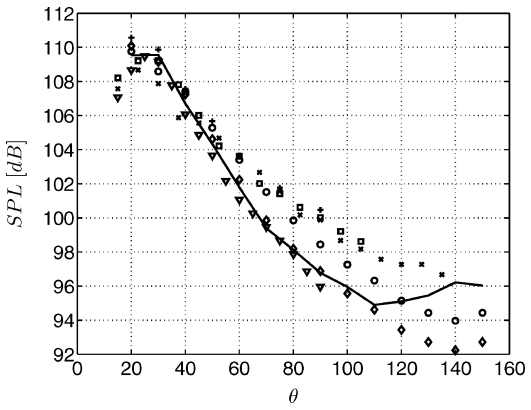

Fig. 23 Sound pressure levels $30D_j$ from the nozzle exit: ——, predicted SPL for jet 1. Experiments are denoted as follows: +, Mollo-Christensen et al.[31] ($M_j = 0.9$, $Re_D = 5.4 \times 10^5$); □, Lush[32] ($M_j = 0.88$, $Re_D = 5.0 \times 10^5$); ×, Tanna[12] ($M_j = 0.9$, $Re_D = 9.1 \times 10^5$); ▽, Stromberg et al.[33] ($M_j = 0.9$, $Re_D = 3600$); ○, Jordan et al.[17] ($M_j = 0.75$, $Re_D = 7.5 \times 10^5$); and ◇, Jordan et al.[17] ($M_j = 0.9$, $Re_D = 9.0 \times 10^5$).

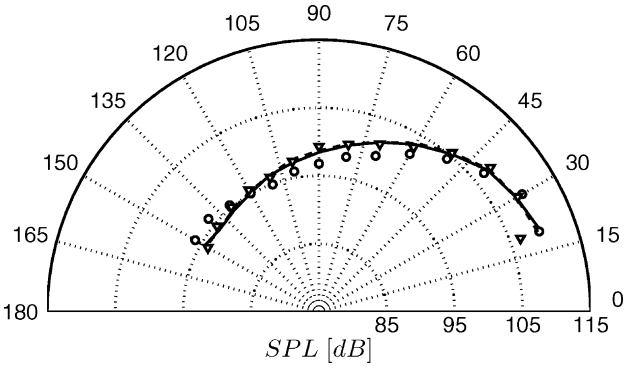

a) $r = 30D_j$

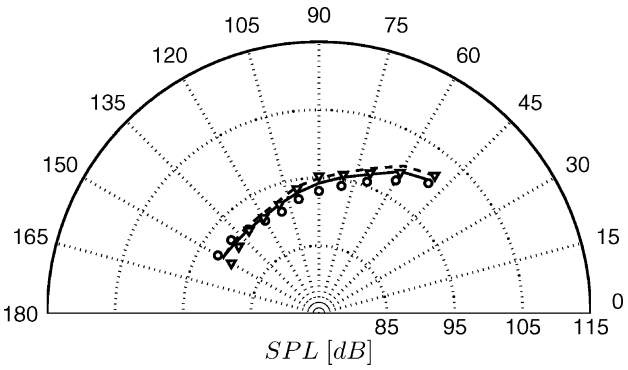

b) $r = 50D_j$

Fig. 24 Comparison of SPL for jets 1 and 2: —— and – – –, measured[17] data for jets 1 and 2, respectively; ○ and △, predicted SPL.

changes in overall levels are virtually not affected by the temperature ratio for the current Mach number, the work by Tanna[12] indicates that there are significant changes in the spectra: the amplitude at very low frequencies increases when the temperature ratio is increased while the amplitude in the high-frequency range decreases. For the current Mach number these two effects cancel, and therefore no changes are visible in the overall levels. Unfortunately, these spectrum effects are not captured because the high-frequency range is filtered by the numerics and the low-frequency range is unresolved.

In summary, the predicted sound pressure levels are for all observers within the 3.0-dB deviation from the measured levels indicated by dashed lines in Figs. 20 and 22 and for most of the observers within a 1.0-dB deviation, which must be considered as a satisfying result. These levels have been obtained directly from the LES/Kirchhoff data without adjustment. Also, the predictions are

obtained for a lower Reynolds number than the measured data, which probably affects the acoustic signature. However, the Reynolds-number effects would probably be most significant in the high-frequency range, which is highly filtered by the numerical method anyway.

VII. Conclusions

Large-eddy simulation of a compressible Mach 0.75 nozzle/jet configuration has been performed. The Reynolds number based on jet velocity and nozzle diameter was 5.0×10^4. Jet simulations were performed at two heating conditions, an unheated jet where the exhaust static temperature was equal to the static temperature of the surrounding air and a heated jet where the nozzle outlet temperature was twice that of the ambient air. Profiles of time and azimuthally averaged flow properties have been compared with data measured by Jordan et al.[16] Although some deviations occur, the results are in general in very good agreement with experiments. The good results are probably attributed to the homogeneity of the mesh used and the fact that a nozzle geometry was included in the calculation domain. Using a combination of Cartesian and polar mesh blocks makes it possible to ensure that cells in the outer regions of the calculation domain are not too large and prevents cells from being clustered in the centerline region.

The maximum levels of turbulence intensities are well captured for both jets. Furthermore, the turbulence anisotropy of the jets is correctly predicted. The initial jet spreading and the potential core lengths are, however, not predicted correctly. Overpredicted $u'v'$ correlations close to the nozzle exit indicate that the degree of mixing is too high, which makes the transition process too efficient, and hence the length of the potential region becomes shorter. This might be caused by a combination of several factors such as lack of subgrid-scale dissipation, the numerical method used, entrainment boundary conditions, and inflow conditions. Of these, the inflow conditions are believed to be the most important.

Two-point space–time correlations were obtained in a number of locations in the shear layer along the nozzle lip line. Correlation curves obtained at $x = L_c$ were in good agreement with experiments.[18] Two-point space–time correlations in the shear layer were used to obtain estimates of integral length scales, integral timescales, and eddy convection velocities. The agreement with corresponding quantities obtained from the measured data was satisfying. Only small differences could be identified in correlations and integral scales for the two jets.

Sound pressure levels in the far field were evaluated with a hybrid approach. Kirchhoff surface integration was utilized for the propagation of sound to far-field locations. Predicted sound pressure levels were in excellent agreement with the levels measured by Jordan et al.[17] for both jets. However, the mesh used fails to capture waves of Strouhal numbers higher than $Sr \simeq 1.2$. This results in a rapid fall-off of the spectrum amplitudes for higher Strouhal numbers. The lower part of the spectra is accurately captured, however. Because the sound pressure levels obtained were in good agreement with the measured levels, capturing the lower part of the spectra seems to be sufficient to represent the main part of the radiated sound. Both measurements and predictions show slightly higher SPL for the heated jet. The increase in SPL is, however, too small to be able to draw any conclusions regarding the effects of the increased temperature ratio on the radiated sound.

Although, the predictions of both near-field statistics and far-field acoustic signature are generally in good agreement with measured data, there are a number of parameters to which the predictions are sensitive. The fact that the predictions have been obtained for a lower Reynolds number than the measured data changes the range of scales present in the jet. This will affect the frequency content of the radiated sound. The inflow conditions affect the initial mixing, and thus the initial shear-layer growth and the potential core lengths are affected. Moreover, because the current effort deals with a subsonic jet, most of the radiated sound is generated in the potential core region, which is highly dependent of the nature of the incoming disturbances. However, both the Reynolds-number effects and the effects of the inflow conditions on the radiated sound are probably noticeable mostly in the high-frequency range, which is significantly filtered by the numerical method. Another uncertainty is related to the location of the Kirchhoff surface. The predicted sound pressure levels are sensitive to the location of the integration surface. The surface has to be placed far enough from the jet to avoid hydrodynamic fluctuations in the surface region but close enough to avoid numerical dissipation of the radiated sound. To accomplish a good compromise, a jet-fitted integration surface has been used. Still the surface location should be considered as a factor of uncertainty.

With a surface integral approach, it is sufficient to use a mesh resolving the main noise generation structures and supporting acoustic waves within the frequency range contributing most to the overall sound pressure levels. However, if the aim were to capture the sound spectra in far-field locations, higher mesh resolution and probably higher-order schemes would be desirable.

Acknowledgment

This work was conducted as part of the European Union 5th Framework Project JEAN (Jet Exhaust Aerodynamics and Noise), Contract G4RD-CT2000-000313.

References

[1]Freund, J., "Noise Sources in a Low-Reynolds-Number Turbulent Jet at Mach 0.9," *Journal of Fluid Mechanics*, Vol. 438, 2001, pp. 277–305.

[2]Mitchell, B., Lele, S., and Moin, P., "Direct Computation of the Sound Generated by Vortex Pairing in an Axisymmetric Jet," *Journal of Fluid Mechanics*, Vol. 383, 1999, pp. 113–142.

[3]Bogey, C., Bailly, C., and Juvé, D., "Computation of the Sound Radiated by a 3-D Jet Using Large Eddy Simulation," AIAA Paper 2000-2009, May 2000.

[4]Mankbadi, R., Shih, S., Hixon, R., and Povinelli, L., "Direct Computation of Jet Noise Produced by Large-Scale Axisymmetric Structures," *Journal of Propulsion and Power*, Vol. 16, No. 2, 2000, pp. 207–215.

[5]Mankbadi, R., "Review of Computational Aeroacoustics in Propulsion Systems," *Journal of Propulsion and Power*, Vol. 15, No. 4, 1999, pp. 504–512.

[6]Freund, J., Lele, S., and Moin, P., "Calculation of the Radiated Sound Field Using an Open Kirchhoff Surface," *AIAA Journal*, Vol. 34, No. 5, 1996, pp. 909–916.

[7]Bogey, C., Bailly, C., and Juvé, D., "Noise Investigation of a High Subsonic, Moderate Reynolds Number Jet Using a Compressible Large Eddy Simulation," *Theoretical and Computational Fluid Dynamics*, Vol. 16, No. 4, 2003, pp. 273–297.

[8]Bogey, C., Bailly, C., and Juvé, D., "Noise Computation Using Lighthill's Equation with Inclusion of Mean Flow–Acoustic Interactions," AIAA Paper 2001-2255, May 2001.

[9]Lighthill, M., "On Sound Generated Aerodynamically, I. General Theory," *Proceedings of the Royal Society of London*, Vol. A211, 1952, pp. 564–587.

[10]Bogey, C., and Bailly, C., "LES of a High Reynolds, High Subsonic Jet: Effects of the Inflow Conditions on Flow and Noise," AIAA Paper 2003-3170, May 2003.

[11]Bodony, D., and Lele, S., "Jet Noise Prediction of Cold and Hot Subsonic Jets Using Large-Eddy Simulation," AIAA Paper 2004-3022, May 2004.

[12]Tanna, H., "An Experimental Study of Jet Noise Part I: Turbulent Mixing Noise," *Journal of Sound and Vibration*, Vol. 50, No. 3, 1977, pp. 405–428.

[13]Shur, M., Spalart, P., Strelets, M., and Travin, A., "Towards the Prediction of Noise from Jet Engines," *International Journal of Heat and Fluid Flow*, Vol. 24, No. 4, 2003, pp. 551–561.

[14]Ffowcs Williams, J., and Hawkings, D., "Sound Generated by Turbulence and Surfaces in Arbitrary Motion," *Philosaphical Transactions of the Royal Society of London*, Vol. A264, 1969, pp. 321–342.

[15]Zhao, W., Frankel, S., and Mongeau, L., "Large Eddy Simulation of Sound Radiation from Subsonic Turbulent Jets," *AIAA Journal*, Vol. 39, No. 8, 2001, pp. 1469–1477.

[16]Jordan, P., Gervais, Y., Valiére, J.-C., and Foulon, H., "Final Results from Single Point Measurements," Lab. d'Etude Aérodynamiques, Project deliverable D3.4, JEAN-EU 5th Framework Programme, G4RD-CT2000-00313, Poitiers, France, April 2002.

[17]Jordan, P., Gervais, Y., Valiére, J.-C., and Foulon, H., "Results from Acoustic Field Measurements," Lab. d'Etude Aérodynamiques, Project deliverable D3.6, JEAN-EU 5th Framework Programme, G4RD-CT2000-00313, Poitiers, France, July 2002.

[18]Jordan, P., and Gervais, Y., "Modeling Self and Shear Noise Mechanisms in Anisotropic Turbulence," AIAA Paper 2003-8743, May 2003.

[19]Power, O., Kerhervé, F., Fitzpatrick, J., and Jordan, P., "Measurements of Turbulence Statistics in High Subsonic Jets," AIAA Paper 2004-3021, May 2004.

[20]Erlebacher, G., Hussaini, M., Speziale, C., and Zang, T., "Toward the Large-Eddy Simulation of Compressible Turbulent Flows," *Journal of Fluid Mechanics*, Vol. 238, 1992, pp. 155–185.

[21]Lyrintzis, A., "Review: The Use of Kirchhoff's Method in Computational Aeroacoustics," *Journal of Fluids Engineering*," Vol. 116, Dec. 1994, pp. 665–676.

[22]Rahier, G., Prieur, J., Vuillot, F., Lupoglazoff, N., and Biancherin, A., "Investigation of Integral Surface Formulations for Acoustic Predictions of Hot Jets Starting from Unsteady Aerodynamic Simulations," AIAA Paper 2003-3164, May 2003.

[23]Eriksson, L.-E., "Development and Validation of Highly Modular Flow Solver Versions in G2DFLOW and G3DFLOW," Volvo Aero Corp., Internal Rept. 9970-1162, Trollhättan, Sweden, 1995.

[24]Mårtensson, H., Eriksson, L.-E., and Albråten, P., "Numerical Simulations of Unsteady Wakeflow," International Symposium on Air Breathing, Paper 9370-309, Aug. 1991.

[25]Wollblad, C., Eriksson, L.-E., and Davidson, L., "Semi-Implicit Preconditioning for Wall-Bounded Flow," AIAA Paper 2004-2135, June 2004.

[26]Tam, C., and Webb, J., "Dispersion-Relation-Preserving Finite Difference Schemes for Computational Acoustics," *Journal of Computational Physics*, Vol. 107, No. 2, 1993, pp. 262–281.

[27]Billson, M., "Computational Techniques for Turbulence Generated Noise," Ph.D. Dissertation, Div. of Thermo and Fluid Dynamics, Chalmers Univ. of Technology, Gothenburg, Sweden, June 2004.

[28]Andersson, N., Eriksson, L.-E., and Davidson, L., "Large-Eddy Simulation of a Mach 0.75 Jet," AIAA Paper 2003-3312, May 2003.

[29]Andersson, N., "A Study of Mach 0.75 Jets and Their Radiated Sound Using Large-Eddy Simulation," Licentiate Thesis, Div. of Thermo and Fluid Dynamics, Chalmers Univ. of Technology, Gothenburg, Sweden, Oct. 2003.

[30]Hinze, J., *Turbulence*, 2nd ed., McGraw–Hill, New York, 1975, Chap. 6.

[31]Mollo-Christensen, E., Kolpin, M. A., and Martuccelli, J. R., "Experiments on Jet Flows and Jet Noise Far-Field Spectra and Directivity Patterns," *Journal of Fluid Mechanics*, Vol. 18, 1964, pp. 285–301.

[32]Lush, P., "Measurements of Subsonic Jet Noise and Comparison with Theory," *Journal of Fluid Mechanics*, Vol. 46, 1971, pp. 477–500.

[33]Stromberg, J., McLaughlin, D., and Troutt, T., "Flow Field and Acoustic Properties of a Mach Number 0.9 Jet at a Low Reynolds Number," *Journal of Sound and Vibration*, Vol. 72, No. 2, 1980, pp. 159–176.

[34]Jiang, X., Avital, E., and Luo, K., "Sound Generation by Vortex Pairing in Subsonic Axisymmetric Jets," *AIAA Journal*, Vol. 42, No. 2, 2004, pp. 241–248.

[35]Crighton, D., "Basic Principles of Aerodynamic Noise Generation," *Progress in Aerospace Sciences*, Vol. 16, No. 1, 1975, pp. 31–96.

D. Gaitonde
Associate Editor